# ATLAS NOTE

ATLAS-CONF-2013-027

March 10, 2013

# Search for Higgs bosons in Two-Higgs-Doublet models in the $H \to WW \to e\nu\mu\nu$ channel with the ATLAS detector

The ATLAS Collaboration

## Abstract

The Higgs-like boson observed at the LHC with a mass of approximately 125 GeV could be part of an extended scalar sector originating from two complex Higgs doublets. The analysis presented in this note investigates the possibility of a Two-Higgs-Doublet model (2HDM) being realized in nature by searching for evidence of a second, heavier, CP-even scalar boson in the $H \to WW^{(*)} \to e^- \bar{\nu}_e \mu^+ \nu_\mu / e^+ \nu_e \mu^- \bar{\nu}_\mu$ decay mode. The analysis is based on proton-proton collision data at a centre-of-mass energy of 8 TeV collected with the ATLAS detector and corresponding to an integrated luminosity of $13.0\,\text{fb}^{-1}$. Artificial neural network techniques are used to maximise the sensitivity. No evidence for a second scalar boson is found in the investigated mass range between 135 and 300 GeV. Exclusion limits on type-I and type-II 2HDMs are set as a function of the two mixing angles $\alpha$ and $\beta$ as well as the mass $m_H$ of the heavier scalar boson. For the limits the signal hypothesis includes the Higgs-like boson at 125 GeV and assumes that it is the light scalar $h$ of a 2HDM, while the null hypothesis assumes no Higgs boson at all.

# 1  Introduction

The experiments ATLAS and CMS at the Large Hadron Collider (LHC) have observed a Higgs-like boson at a mass of approximately 125 GeV [1, 2]. To-date, all measurements concerning the production rates, the branching ratios and kinematic distributions are compatible with this particle being the Higgs boson predicted by the Standard Model (SM). The mass of the observed state is also consistent with constraints on the Higgs boson mass obtained from electroweak precision measurements [3].

The so-called Brout-Englert-Higgs (BEH) mechanism [4, 5, 6] implements the spontaneous breaking of the electroweak gauge symmetry and thereby explains the mass generation of elementary particles, in particular the mass of the weak gauge bosons, but also the mass of the fermions via the Yukawa coupling. The resulting field and the associated Higgs boson are essential to formulate a consistent and coherent theory of electroweak interactions.

The BEH mechanism of the SM postulates the existence of one doublet of complex fields, yielding four degrees of freedom, three of which provide the longitudinal polarisation modes of the massive weak gauge bosons, while one degree of freedom materialises as the Higgs boson. In this form the SM BEH mechanism constitutes only a minimal configuration to implement the breaking of the electroweak symmetry and the generation of particle masses. A simple extension of the SM Higgs sector is given by the addition of a second complex Higgs doublet [7], giving rise to five Higgs bosons: two CP-even scalar fields $h$ and $H$, one pseudoscalar $A$ (CP-odd), and two charged fields $H^{\pm}$. These Two-Higgs-Doublet models (2HDM) are phenomenologically interesting since they can explain the generation of the baryon asymmetry in the universe [8] and are an important ingredient of axion models that are designed to explain its the dark matter content [9]. Finally, the minimal supersymmetric SM [10] contains two Higgs doublets as well. Four different types of 2HDMs can be distinguished, depending on the different coupling of the two scalar fields $h$ and $H$ to fermions and weak gauge bosons. In type-I models all quarks couple to just one of the Higgs doublets, while in type-II models the right-handed up-type quarks couple to one Higgs doublet and the right-handed down-type quarks to the other doublet. Type-III and type-IV models differ only from type-I and type-II models in their couplings to the leptons. Since the analysis presented in this note is not sensitive to the leptonic couplings, type-III and type-IV models are not considered. Recent detailed reviews on 2HDMs can be found in Refs. [11, 12]. Since the discovery of the Higgs-like boson at the LHC, 2HDMs have attracted much attention in phenomenological studies [13, 14, 15, 16, 17], which provide a strong incentive for dedicated experimental investigations in this direction. Searches for generic 2HDMs have been performed by the CDF collaboration at the Tevatron [18, 19]. The rate of the Higgs-like boson at 125 GeV in the two-photon channel provides also constraints on 2HDMs [20], mainly reducing the parameter space of type-II models.

The analysis presented in this note investigates the possibility that the boson observed by the ATLAS and CMS experiments at a mass of 125 GeV originates from a Higgs boson that is part of a 2HDM. In particular, it is assumed that the observed particle is the low mass Higgs $h$ of the 2HDM. The analysis searches for additional signal contributions by the higher mass CP-even boson $H$ of the model. Both Higgs bosons are reconstructed in the $h\,/\,H \rightarrow WW^{(*)} \rightarrow e^{-}\bar{\nu}_{e}\mu^{+}\nu_{\mu}\,/\,e^{+}\nu_{e}\mu^{-}\bar{\nu}_{\mu}$ decay channel and their contributions are both part of the signal hypothesis, while the null hypothesis assumes no Higgs boson at all. The pseudoscalar $A$ does not decay to pairs of vector bosons and therefore does not contribute to the signal rates directly. Indirect contributions, for example via $A \rightarrow \tau^{+}\tau^{-}$ decays, are neglected, which leads to a slight underestimation of the sensitivity. The following two production modes of Higgs bosons are considered: the gluon fusion process, see Fig. 1(a) and the vector-boson-fusion (VBF) process, see Fig. 1(b). To be sensitive to both production mechanisms the analysis considers two different final states. In the first channel, two charged leptons and large missing transverse momentum $E_{\mathrm{T}}^{\mathrm{miss}}$ are required (0-jet channel), and in the second channel, which is sensitive to the VBF process, two high-$p_{\mathrm{T}}$ jets (2-jet channel) are reconstructed in addition.

Figure 1: Leading order Feynman diagrams for Higgs boson production via (a) gluon fusion and (b) vector boson fusion (VBF).

The expected signal rates depend on the mixing angles $\alpha$ and $\beta$ of the two Higgs doublets and the mass $m_H$ of the higher mass state $H$. Different signal hypotheses characterized by different values of $\cos\alpha$, $\tan\beta$, and $m_H$ are tested using the CLs method. Artificial neural networks (NN) are used to enhance the sensitivity by combining the information contained in various kinematic and angular variables. The mass interval of $135 < m_H < 300$ GeV is probed in the hypothesis tests.

## 2    Data samples and samples of simulated events

The analysis described in this note uses LHC $pp$ collision data at a centre-of-mass energy of 8 TeV collected with the ATLAS detector [21] between April and September 2012. The selected events were recorded based on single-electron and single-muon triggers. Stringent detector and data quality requirements are applied, resulting in a dataset corresponding to an integrated luminosity of 13.0 fb$^{-1}$.

The ATLAS detector is built from a set of cylindrical subdetectors, which cover almost the full solid angle[1] around the interaction point.

ATLAS is composed of an inner tracking system close to the interaction point, surrounded by a super-conducting solenoid providing a 2 T axial magnetic field, electromagnetic and hadronic calorimeters, and a muon spectrometer. The electromagnetic calorimeter is a lead liquid-argon sampling calorimeter (LAr) with high granularity. An iron-scintillator tile calorimeter provides hadronic energy measurements in the central pseudorapidity range. The endcap and forward regions are instrumented with LAr calorimeters for both electromagnetic and hadronic energy measurements. The muon spectrometer consists of three large superconducting toroids, a system of trigger chambers, and precision tracking chambers.

In the analysis, the production of the two CP-even Higgs bosons $h$ and $H$ of the 2HDM is modelled with samples of simulated events generated for SM Higgs boson studies, while scaling the production cross sections according to the parameters of the 2HDM. The mass of the light Higgs boson $h$ is fixed to $m_h = 125$ GeV in simulation. The mass of the heavy Higgs boson $H$ is varied between 135 and 300 GeV, using steps of 5 GeV between 135 and 200 GeV and steps of 20 GeV between 200 and 300 GeV. In the search region, the natural width of the Higgs bosons is negligible with respect to the experimental resolution. The samples of simulated events for the Higgs boson gluon fusion and the VBF processes are generated with the POWHEG [22, 23] package, interfaced to PYTHIA [24] for showering and hadronisation. The associated $WH$ and $ZH$ production processes are modelled using PYTHIA, with the Higgs boson decaying to $W^+W^-$, while the $W$ and $Z$ bosons decay inclusively to all modes. At particle level

---

[1]ATLAS uses a right-handed coordinate system with its origin at the nominal interaction point in the centre of the detector and the $z$-axis along the beam direction. The $z$-axis is parallel to the anti-clockwise beam viewed from above. The pseudorapidity $\eta$ is defined as $\eta = -\ln[\tan(\theta/2)]$, where the polar angle $\theta$ is measured with respect to the $z$-axis. The azimuthal angle $\phi$ is measured with respect to the $x$-axis, which points towards the centre of the LHC ring. Transverse momentum and energy are defined as $p_T = p\sin\theta$ and $E_T = E\sin\theta$, respectively. The $\Delta R$ distance is defined as $\Delta R = \sqrt{(\Delta\eta)^2 + (\Delta\phi)^2}$.

an event filter is applied that requires two charged leptons from the decay of the Higgs boson. The CT10 [25] set of parton distribution functions (PDF) is used for the gluon-fusion, the VBF, and the *WH/ZH* samples.

The cross section of the gluon-fusion process has been computed with next-to-next-to-leading order (NNLO) QCD corrections [26, 27, 28], next-to-leading order (NLO) electroweak corrections [29, 30], and corrections arising from the resummation of soft-gluon terms [31]. When rescaling the SM gluon-fusion cross section to a specific 2HDM, the different scaling of the top-quark-loop and bottom-quark-loop contributions, as well as their interference, is properly accounted for by using calculations that provide the relevant split of these three contributions [32, 33]. The expectation value of VBF Higgs boson events is computed by using theoretical cross-section predictions that include full NLO QCD and electroweak corrections [34, 35, 36] and approximate NNLO QCD corrections [37]. The theoretical cross-sections for the Higgs-strahlung processes *WH* and *ZH* are calculated with NNLO QCD corrections [38] and NLO electroweak corrections [39].

Inclusive *W* and $Z/\gamma^*$ vector boson production in association with jets is simulated using the leading-order (LO) generator ALPGEN version 2.13 [40], showered with HERWIG [41] in connection with the JIMMY [42] underlying event model. *W*+jets and *Z*+jets events with up to five additional partons are generated. The MLM matching scheme [43] is used to remove jets generated by the parton shower and those from the matrix element.

The diboson processes (*WW*, *WZ*, $W\gamma^*$, and *ZZ*) are generated using POWHEG and showered with PYTHIA. An additional contribution to the continuum *WW* background from gluon-initiated diagrams is modelled using gg2WW [44], also interfaced to HERWIG and JIMMY. The matrix element generators MADGRAPH [45] and ALPGEN (interfaced to HERWIG) are used to model $W\gamma^*$ with $m_{\gamma^*} < 7$ GeV and $W\gamma$, respectively. Samples of the *t*-channel single top-quark process are produced with the AcerMC program [46] linked to PYTHIA [24] for showering and hadronisation. The *s*-channel single top-quark process and *Wt* production are generated using MC@NLO version 3.41 [47] and showered with HER-WIG. Samples modelling $t\bar{t}$ pair production are generated with MC@NLO. All top-quark processes are produced with a top-quark mass of 172.5 GeV.

More details on the event generators applied in this analysis and on the theoretical cross-sections used to normalise these samples can be found in Ref. [48], describing the SM Higgs boson analysis in the $H \rightarrow WW^*$ channel.

After the event generation step, all samples are passed through the full simulation of the ATLAS detector [49] based on GEANT4 [50] and are then reconstructed using the same procedure as for collision data. The simulation includes the effect of multiple $pp$ collisions per bunch crossing (pile-up) at a variable rate and the events are weighted to match the conditions of the data sample using the average number of collisions per bunch crossing.

## 3   Object definitions and event selection

Candidate events of the $h/H \rightarrow WW^{(*)} \rightarrow e\nu\mu\nu$ process are recorded using unprescaled single-electron and single-muon triggers with a $p_T$ threshold of 24 GeV. A number of requirements are applied in order to ensure a consistent event quality and to remove mis-reconstructed events. Events are selected if they contain at least one good primary vertex candidate with at least three associated tracks with $p_T > 0.4$ GeV. Non-collision backgrounds are excluded, i.e. cosmic rays passing through the detector, beam backgrounds and instrumental effects like noise bursts in certain parts of the detector. The event selection is based on the identification of electrons, muons and jets and on the reconstruction of $E_T^{miss}$ (missing transverse momentum).

Electron candidates are selected from LAr electromagnetic calorimeter clusters matched to tracks and are reconstructed offline using a Gaussian sum filter algorithm [51]. The energy of an electron candidate

is taken from the calorimeter cluster, while its $\eta$ and $\phi$ are taken from the track. It is required that the track points back to the primary vertex with transverse impact parameter significance (the ratio of the transverse impact parameter to its error) less than 3. The $z$-position of the track has to be compatible with the primary vertex. Electron candidates are excluded if they lie in the pseudorapidity ranges $1.37<|\eta|<1.52$ or $|\eta|>2.47$. The electron candidates are further required to fulfil stringent criteria regarding calorimeter shower shape, track quality, track-cluster matching, and transition radiation energy to ensure high identification quality. Electron candidates are required to be isolated by placing cuts on $\Sigma(p_{\mathrm{T}}^{\mathrm{track}})$, the scalar sum of the transverse momenta of tracks in a cone of $\Delta R = \sqrt{\Delta \eta^2 + \Delta \phi^2} = 0.3$ around the candidate excluding the track associated to the electron candidate, and $\Sigma(p_{\mathrm{T}}^{\mathrm{calo}})$, the scalar sum of the transverse momenta of calorimeter energy deposits for a cone of the same size also excluding the energy deposit associated to the candidate. For an electron candidate the fractional track based isolation, $\Sigma(p_{\mathrm{T}}^{\mathrm{track}})/p_{\mathrm{T}}$ is required to be below 0.16, and this is tightened to 0.12 for candidates with $p_{\mathrm{T}}$ below 25 GeV which have more background, while $\Sigma(p_{\mathrm{T}}^{\mathrm{calo}})/p_{\mathrm{T}}$ is required to be below 0.16. If two electron candidates are reconstructed within a cone of $\Delta R = 0.1$, the candidate the with lower $p_{\mathrm{T}}$ is discarded.

Muons are reconstructed by taking a statistical combination of the matched tracks in the Inner Detector (ID) and in the Muon Spectrometer (MS). The muon candidates are required to have a sufficiently large number of hits in the silicon detector and the Transition Radiation Tracker (TRT). Muon tracks are required to have at least one hit in the pixel detector, and four or more hits in the Semiconductor Tracker (SCT). Tracks are vetoed if they have more than two missing hits in the SCT and pixel detectors, as well as tracks with an excessive number of outlier hits in the TRT. The momentum as measured using the ID is required to agree with the momentum measured using the MS after correcting for the predicted muon energy loss in the calorimeter. Muon candidates are required to have $p_{\mathrm{T}} > 15$ GeV and $|\eta| < 2.4$, and must satisfy a similar isolation and the same impact parameter cuts as electron candidates. The required calorimeter isolation is $\Sigma(p_{\mathrm{T}}^{\mathrm{calo}})/p_{\mathrm{T}} < 0.014/\mathrm{GeV} \cdot p_{\mathrm{T}} - 0.15$ and $\Sigma(p_{\mathrm{T}}^{\mathrm{calo}})/p_{\mathrm{T}} < 0.20$, while for the track based isolation $\Sigma(p_{\mathrm{T}}^{\mathrm{track}})/p_{\mathrm{T}} < 0.01/\mathrm{GeV} \cdot p_{\mathrm{T}} - 0.105$ and $\Sigma(p_{\mathrm{T}}^{\mathrm{track}})/p_{\mathrm{T}} < 0.15$ is required. If an electron lies in a cone of $\Delta R = 0.1$ around a reconstructed muon, the electron candidate is ignored.

The reconstruction, identification and trigger efficiencies of electrons and muons were measured using tag-and-probe methods on samples enriched with $Z \to \ell\ell$, $J/\psi \to \ell\ell$, or $W^{\pm} \to \ell\nu$ ($\ell = e, \mu$) events.

Jets are reconstructed from topological clusters using the anti-$k_t$ algorithm [52] with the size parameter $R = 0.4$. The response of the calorimeter is corrected through a $p_{\mathrm{T}}$- and $\eta$-dependent factor, which is derived from simulated events and is applied to each jet to provide an average energy scale correction [53]. The selected jets are required to have $p_{\mathrm{T}} > 25$ GeV at the hadronic energy scale. This threshold is increased to 30 GeV in the forward region ($|\eta| > 2.5$) which is more sensitive to reconstruction issues arising from pile-up events. Only jets within $|\eta| < 4.5$ are used. To reject jets from pile-up events, a quantity called the jet-vertex fraction (JVF) is defined as the ratio of $\sum p_{\mathrm{T}}$ for all tracks within the jet that originate from the primary vertex associated to the hard-scattering collision to the $\sum p_{\mathrm{T}}$ of all tracks matched to the jet; and it is required that JVF $> 0.5$. For jets having no matched tracks, this criteria is omitted. Selected jets are identified as $b$-quark jets by reconstructing secondary and tertiary vertices from the tracks associated with each jet and combining lifetime related information with a NN [54]. The identification requirement has an efficiency of 85% for $b$-quark jets in $t\bar{t}$ events. If a jet candidate lies within a cone of $\Delta R = 0.3$ around a reconstructed electron, the jet candidate is ignored.

The $\vec{E}_{\mathrm{T}}^{\mathrm{miss}}$ is reconstructed starting from topological energy clusters in the calorimeters, with corrections for measured muons [55]. To reduce the effect of mismeasurements of jets and leptons leading to artificial $E_{\mathrm{T}}^{\mathrm{miss}}$, the event selection uses the $E_{\mathrm{T,rel}}^{\mathrm{miss}}$ variable which is defined as

$$
E_{\mathrm{T,rel}}^{\mathrm{miss}} = \begin{cases} E_{\mathrm{T}}^{\mathrm{miss}} \sin(\Delta\phi_{\mathrm{min}}) & \text{if } \Delta\phi_{\mathrm{min}} < \pi/2 \\ E_{\mathrm{T}}^{\mathrm{miss}} & \text{if } \Delta\phi_{\mathrm{min}} \geq \pi/2 \end{cases} \tag{1}
$$

4

Table 1: The expected number of signal and background events for $13\,\text{fb}^{-1}$ of integrated luminosity in the 0-jet channel and in the 2-jet channel after all selection cuts. The event yield of a potential signal is illustrated for a light Higgs boson with $m_\text{h} = 125$ GeV and a heavy Higgs boson with $m_\text{H} = 150$ GeV in a type-I 2HDM with $\tan\beta = 3$ and $\alpha = \pi/2$. The $W$+jets background is entirely determined from data [48]. The uncertainties quoted in the table are determined from the sum in quadrature of two sources: the total rate uncertainty, see Table 3, and the corresponding cross-section uncertainties. Since the $W$+jets background is derived from collision data the uncertainties of the data-driven estimation are used.

| Process | 0 jet | 2 jet | Top control region | WW control region |
|---|---|---|---|---|
| Signal ($m_h = 125$ GeV) | $2.55 \pm 0.50$ | $5.52 \pm 0.71$ | $1.35 \pm 0.19$ | $0.76 \pm 0.13$ |
| Signal ($m_H = 150$ GeV) | $470 \pm 140$ | $76 \pm 19$ | $20.9 \pm 5.7$ | $16.1 \pm 3.9$ |
| $WW/WZ/ZZ/W\gamma/W\gamma*$ | $1140 \pm 290$ | $63 \pm 18$ | $22.1 \pm 6.2$ | $1170 \pm 310$ |
| $Z/\gamma^* +$ jets | $41 \pm 15$ | $194 \pm 72$ | $84 \pm 31$ | $15.7 \pm 6.4$ |
| $W$+jets | $135 \pm 58$ | $23.4 \pm 9.7$ | $18.3 \pm 7.6$ | $78 \pm 32$ |
| $t\bar{t}/tW/tb/tqb$ | $175 \pm 49$ | $168 \pm 77$ | $1760 \pm 440$ | $313 \pm 97$ |
| Total background | $1490 \pm 420$ | $450 \pm 180$ | $1890 \pm 480$ | $1580 \pm 450$ |
| S/B | 0.31 | 0.18 | – | – |
| Observed | 1815 | 483 | 1986 | 1725 |

where $\Delta\phi_\text{min}$ is the minimum separation $\phi$ angle between a lepton or a jet with $p_\text{T} > 25$ GeV and $E_\text{T}^\text{miss}$.

The following pre-selection requirements for $h/H \to WW^{(*)} \to e\nu\,\mu\nu$ candidates are imposed. They are the same as for the SM $H \to WW^{(*)}$ analysis [48]. Exactly two leptons of different flavour (electron or muon) and opposite charge are required. The lepton with the highest $p_\text{T}$ is called the leading lepton $\ell_1$ and must have $p_\text{T} > 25$ GeV, while the second lepton $\ell_2$ fulfils $p_\text{T} > 15$ GeV. The invariant mass of the two leptons $m(\ell_1\ell_2)$ is required to be larger than 10 GeV. The $E_\text{T,rel}^\text{miss}$ is required to be at least 25 GeV. This provides a strong suppression against multijet production via QCD processes and against the $Z$+jets background which originates predominantly from the $Z \to \tau^+\tau^-$ decay channel.

After the preceding cuts the events are divided into two analysis channels: the 0-jet channel, in which exactly zero jets are required, and the 2-jet channel, which features exactly two jets. In the 0-jet channel there is a requirement on the absolute value of the difference in the azimuth angle $\phi$ of the two leptons, $|\Delta\phi(\ell_1, \ell_2)| < 2.4$, and in addition $m(\ell_1\ell_2) < 75$ GeV is required. These two cuts remove background in regions where only a small signal contribution is expected, such that the training of the NN can be focused on the more challenging phase space.

In the 2-jet channel events containing a $b$-tagged jet are rejected in order to suppress backgrounds involving top-quarks. The two jets are required to lie in opposite pseudorapidity hemispheres, $\eta(j_1) \times \eta(j_2) < 0$, and $m(\ell_1\ell_2) < 80$ GeV. Another cut is placed on the transverse mass $m_\text{T}$ which is defined as

$$m_\text{T} = \sqrt{(E_\text{T}(\ell_1\ell_2) + E_\text{T}(\nu\nu))^2 - (\vec{p}_\text{T}(\ell_1\ell_2) + \vec{E}_\text{T}^\text{miss})^2} \tag{2}$$

where $E_\text{T}(\ell_1\ell_2) = \sqrt{\vec{p}_\text{T}^2(\ell_1\ell_2) + m^2(\ell_1\ell_2)}$ and $E_\text{T}(\nu\nu) = \sqrt{(E_\text{T}^\text{miss})^2 + m^2(\ell_1\ell_2)}$. It is required that $m_\text{T} < 180$ GeV.

Table 1 shows the event yield of background and signal in the 0-jet channel and in the 2-jet channel after all selection cuts. The signal was split into two rows to distinguish between the light Higgs boson at $m_\text{h} = 125$ GeV and the heavy Higgs boson at $m_\text{H} = 150$ GeV in the 2HDM. The lowermost row

shows the observed numbers of events in the data. The diboson background ($WW/WZ/ZZ/W\gamma/W\gamma*$), the $Z/\gamma^*$ + jets background and the top-quark background ($t\bar{t}/tW/tb/tqb$) are estimated by using the theoretical cross sections, detector acceptances from simulated events, and data-driven correction factors for identification and reconstruction efficiencies. In the subsequent statistical analysis the *a-priori* estimates are re-evaluated in the maximum-likelihood fit to the NN-discriminants and the event yield in a specifically defined top-quark control region. In this fit the top-quark background is entirely free to float, while the diboson and $Z/\gamma^*$ + jets backgrounds are floating within the uncertainties of the *a-priori* estimate given in Table 1.

The $W$+jets background is estimated using a data-driven technique [48]. A control sample is defined by one lepton that satisfies all identification requirements as defined in the main analysis and one so-called anti-identified lepton that fails these criteria, but passes a looser selection. Except for the lepton identification the events in the $W$+jets control sample pass all other selections as required for the signal samples. To obtain an estimate of the number of $W$+jets in the signal sample, the efficiency $\epsilon_{\text{fake}}$ to misidentify an anti-identified lepton as a lepton has to be accounted for. A dijet data sample is used to determine $\epsilon_{\text{fake}}$ as a function of the $p_T$ of the anti-identified lepton. Residual contributions of leptons originating from $W$ and $Z$ decays are subtracted.

## 4 Signal and background discrimination

To separate 2HDM Higgs boson signal events from background in the $WW^{(*)}$ channel, several kinematic variables are combined to one discriminant in each of the two analysis channels by employing NNs. The NeuroBayes [56] tool is used for preprocessing the input variables and for the training of the NNs. A large number of input variables is studied, but only the highest-ranking variables are chosen for the training of the NNs. The ranking of the variables is automatically determined as part of the preprocessing step and is independent of the training procedure [57].

As a result of this optimisation procedure in the 0-jet channel, six kinematic variables are identified that serve as inputs to three NNs trained at three different Higgs boson mass points: $m_{\text{H}}$ = 150 GeV, 180 GeV, and 240 GeV. Dedicated studies showed that the NNs at these three mass points achieve the same sensitivity in terms of the expected exclusion contours in the $\cos\alpha$–$m_H$ plane as a large number of NNs that are trained with a spacing of 5 GeV in $m_H$. The physical reason for this is the relatively low mass resolution in the $H \rightarrow WW^{(*)} \rightarrow \ell^+\nu\ell^-\bar{\nu}$ channel of approximately 20 GeV. It was further studied that the addition of more variables to the NNs would lead only to an improvement well below 1% in the expected CLs values across the $\cos\alpha$–$m_H$ plane. In the same way nine variables are selected in the 2-jet channel.

The selected variables are listed and explained in Table 2. The two most important input variables for the NN in the 0-jet channel trained at $m_{\text{H}}$ = 150 GeV are $m(\ell_1\ell_2)$ and $m_{\text{T}}$, while the two most important input variables for the NN in the 2-jet channel are $m(j_1 j_2)$ and $m(\ell_1\ell_2)$.

The modelling of the input variables is checked in two control regions that are enriched with the dominating backgrounds: diboson production and $t\bar{t}$ production. The $t\bar{t}$ control region is obtained by requiring at least one $b$-tagged jet. In the final statistical analysis, the $t\bar{t}$-enriched control sample is included in order to determine the rate of $t\bar{t}$ events in situ. The diboson control region is defined by all events passing the full event selection except the cut on $m(\ell_1\ell_2)$. Rather than $m(\ell_1\ell_2) < 75$ GeV it is required that $m(\ell_1\ell_2) > 80$ GeV. To reduce the $Z/\gamma^*$ + jets background one additionally requires that $p_{\text{T}}(\ell_1\ell_2) > 30$ GeV. The two most important input variables of the two analysis channels are shown in Fig. 2 in their respective control regions. Good modelling of the important diboson and $t\bar{t}$ backgrounds is found.

6

Table 2: Input variables used for the NNs in the 0-jet and 2-jet channels. The definitions of the variables use the terms *leading lepton* and *leading jet*, defined as the lepton/jet with the highest $p_\mathrm{T}$.

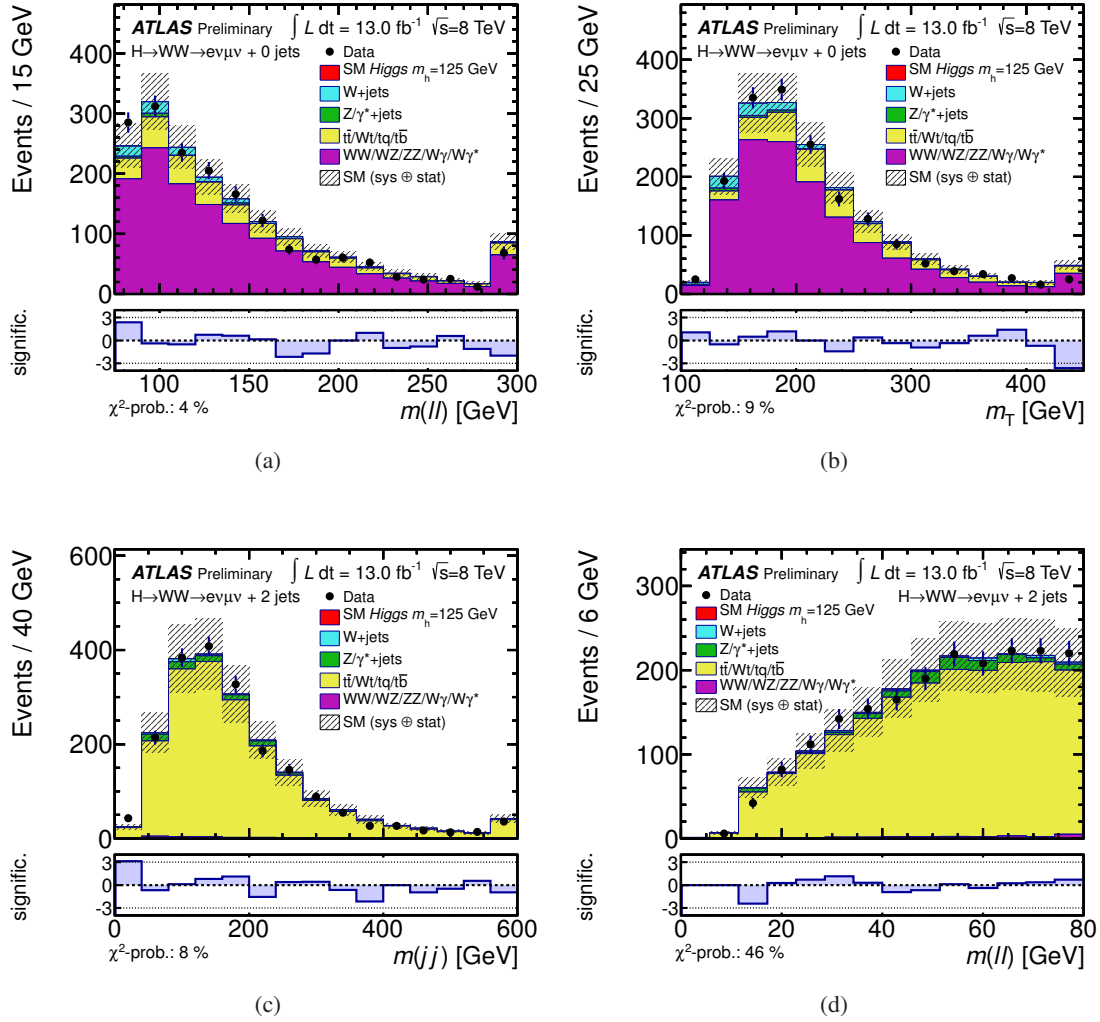| | Variables used in the 0-jet channel and the 2-jet channel |
|---|---|
| $\|\eta(\ell_1)\|$ | The absolute value of the pseudorapidity of the leading lepton. |
| $m_\mathrm{T}$ | The transverse mass of the lepton-$E_\mathrm{T}^{\mathrm{miss}}$ system, as defined in Equation 2. |
| $m(\ell_1\ell_2)$ | The invariant mass of the dilepton system. |
| | **Variables used in the 0-jet channel only** |
| $p_\mathrm{T}(\ell_1\ell_2)$ | The transverse momentum of the dilepton system. |
| $E_\mathrm{T,rel}^{\mathrm{miss}}$ | The projection of the calorimeter-based missing transverse momentum. |
| $\|\Delta Y(\ell_1\ell_2)\|$ | The absolute value of the rapidity differences of the two charged leptons. |
| | **Variables used in the 2-jet channel only** |
| $p_\mathrm{T}(\ell_2)$ | The transverse momentum of the second-leading lepton. |
| $p_\mathrm{T}(j_1)$ | The transverse momentum of the leading jet. |
| $m(j_1)$ | The mass of the leading jet. |
| $\cos\theta(\ell_1,\ell_2)$ | The cosine of the angle between the two charged leptons. |
| $m(j_1 j_2)$ | The invariant mass of the dijet system. |
| $p_\mathrm{T}^{\mathrm{tot}}$ | The total transverse momentum, defined as the magnitude of the vector sum of the transverse momenta of the two jets, the two leptons and the missing transverse momentum: $p_\mathrm{T}^{\mathrm{tot}} = \|\mathbf{p}_\mathrm{T}^{\mathrm{tot}}\| = \|\mathbf{p}_\mathrm{T}^{\ell 1} + \mathbf{p}_\mathrm{T}^{\ell 2} + \mathbf{p}_\mathrm{T}^{j1} + \mathbf{p}_\mathrm{T}^{j2} + \mathbf{p}_\mathrm{T}^{\mathrm{miss}}\|$. |

Figure 2: Distributions of the two highest-ranking input variables of the NN optimised for $m_H = 150$ GeV in the diboson control region, (a) and (b), and in the $t\bar{t}$ control region, (c) and (d). The distributions observed in collision data are compared to a model based on simulated events for which the contribution of each process is normalised to the fitted event rate. The significance of deviations between the model prediction and the observed data is shown in the lower histograms, following [58]. When computing the significance only statistical uncertainties are taken into account.
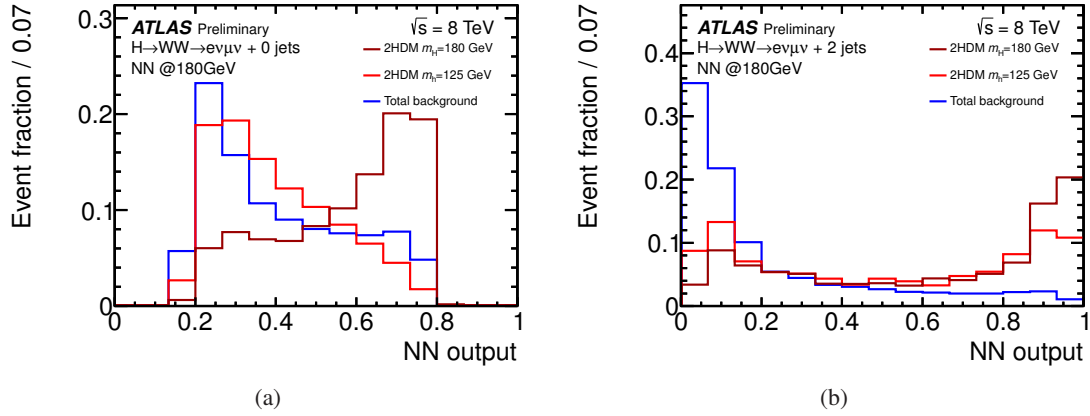
Figure 3: Normalised discriminant distributions (templates) obtained for the NN optimised at $m_H$ = 180 GeV for the 2HDM signal and background, (a) in the 0-jet channel and (b) in the 2-jet channel. The distributions are normalised to unit area.

Once a set of variables has been chosen based on the criteria outlined above, the analysis proceeds with the training of the NNs using a three-layer feed-forward architecture. Bayesian regularisation techniques are applied for the training process to damp statistical fluctuations in the training sample and to avoid overtraining. The ratio of signal to background events in the training is chosen to be 1:1, while the different background processes are weighted according to the number of expected events. The resulting distributions of the 2HDM signal and the total background normalised to unit area are shown in Fig. 3 for the NN optimised at $m_H$ = 180 GeV. The shape of the NN discriminant of the light Higgs boson $h$ in a 2HDM is the same as the one of a pure SM Higgs boson. Only the predicted rate is changed.

After the training is completed, the modelling of the NN-discriminant distributions is checked in the $t\bar{t}$-enriched control region. One example of these cross-check distributions is shown in Fig. 4. The agreement between the model and the observed data is very good, and the next step of the analysis is the application of the NNs to the events in the signal samples. The corresponding distributions of the NN discriminants are shown in Fig. 5. The distributions observed in collision data are compared to a model
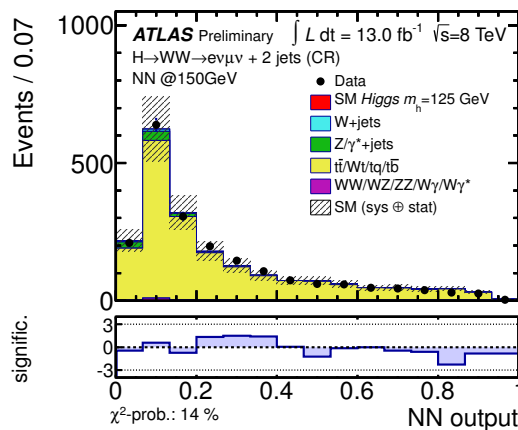


Figure 4: Discriminant distribution obtained with the NN optimised for $m_H$ = 150 GeV with the standard training sample, but evaluated in the $t\bar{t}$ enriched control region in which at least one $b$-tagged jet is required. The contribution of each process is normalised to the fitted event rate.

9

based on simulated events for which the contribution of each process is normalised to the fitted event rates including the SM Higgs boson. The fit is performed to the NN-discriminant distributions in 5(a) and 5(b), simultaneously. The fit results are applied to all other distributions in the signal region as well. The fitted value of the SM Higgs boson event yield is compatible with that measured in the SM analysis in the $WW^*$ channel [48].

To cover the mass range of a potential heavy Higgs boson $H$ from 135 GeV to 300 GeV the three NNs are applied in the following sub-ranges: the NN trained at $m_H = 150$ GeV is evaluated at the mass points from 135 GeV to 160 GeV; the NN trained at $m_H = 180$ GeV is applied in the range from 165 GeV to 200 GeV; and the NN trained at $m_H = 240$ GeV is used at the mass points from 220 GeV to 300 GeV. The evaluation of the background samples and the observed data remains the same for each NN, and only the distributions of the 2HDM Higgs boson samples vary from mass point to mass point. The statistical analysis of the resulting discriminant distributions is discussed in section 6.

The distributions of the input variables are checked in the signal regions by comparing the data to the distributions predicted by the model of simulated events normalised to the fitted event rates of the different components, as described above. The distributions of the two most important variables in the 0-jet and 2-jet channels are shown in Fig. 6. A good agreement between data and the SM prediction is found.
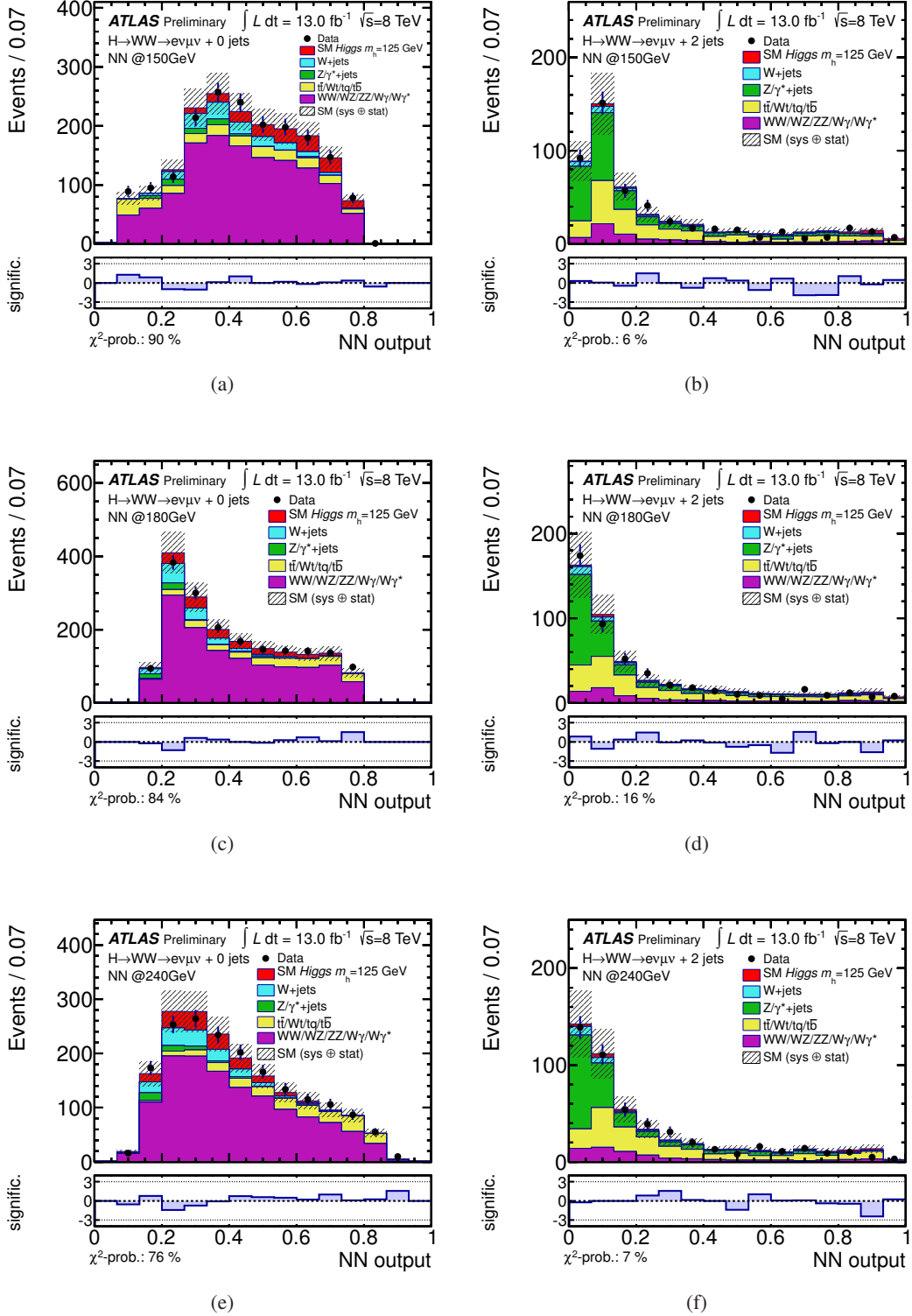
Figure 5: Discriminant distributions obtained from the NNs for three different Higgs boson mass points in the 0-jet and the 2-jet channel. The distributions observed in collision data are compared to a model based on simulated events for which the contribution of each process is normalised to the fitted event rates including the SM Higgs boson. The fit is performed to the NN-discriminant distributions in (a) and (b) and the fit results are applied to the other distributions as well. The fitted value of the SM Higgs boson event yield is compatible with that measured in the SM analysis in the $WW^*$ channel [48]. The shape of the NN discriminant of the SM Higgs is the same as the one of the light Higgs boson $h$ in a 2HDM with $m_h = 125$ GeV.

11
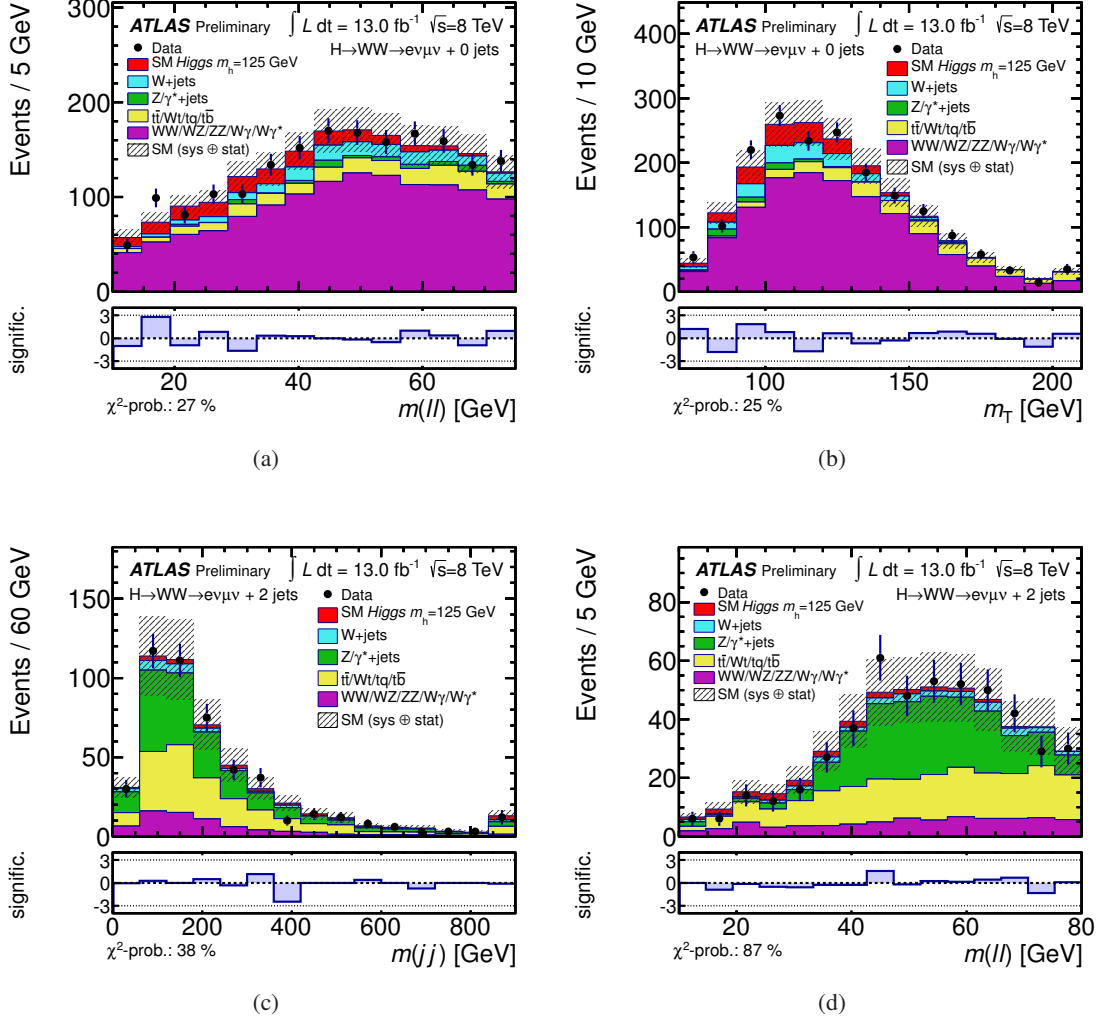
Figure 6: Distributions of the two highest-ranking input variables of the NN optimised for $m_H = 150$ GeV in the signal region of the 0-jet channel, (a) and (b), and in the signal region of the 2-jet channel, (c) and (d). The distributions observed in collision data are compared to a model based on simulated events for which the contribution of each process is normalised to the fitted event rates including the SM Higgs boson. The fit is performed to the NN-discriminant distributions in Figs. 5(a) and (b). The fitted value of the SM Higgs boson event yield is very well compatible with that measured in the $H \rightarrow WW^*$ SM analysis [48]. The significance of deviations between the model prediction and the observed data is shown in the lower histograms, following [58]. When computing the significance only statistical uncertainties are taken into account.

# 5 Systematic uncertainties

Systematic uncertainties in the normalisation of the different backgrounds, on the signal acceptance, and on the shape of the NN-discriminant distributions for signal and background processes reduce the sensitivity of the search for Higgs boson production. Systematic uncertainties arise due to the limited understanding of the residual differences between data and Monte Carlo simulations for the reconstruction and energy calibration of jets, electrons, and muons. Other sources of systematic uncertainties are due to the modelling of physics processes in simulations. All uncertainties are fully propagated through the entire analysis. The following categories of systematic uncertainties are considered:

**Jet modelling**   The main source of uncertainty on the modelling of jets comes from the jet energy scale (JES) [59]. For the jet definition applied in this analysis, the JES uncertainty varies from 2% to 14% as a function of $p_T$ and $\eta$. An additional contribution to the JES uncertainty is caused by pile-up effects and ranges from less than 1% to 4% as a function of jet $p_T$ and $\eta$. For $b$-quark induced jets an additional JES uncertainty of 0.8% to 2.5%, depending on the jet $p_T$, is added in quadrature to the JES uncertainty. Scale factors, determined from collision data [60], are applied to correct the $b$-tagging performance in simulated events to match the data. The uncertainties in the scale factors vary from 10% to 20% for $b$-jets. For light-quark jets, the mis-tagging uncertainty ranges from 20% to 50% as a function of jet $p_T$ and $\eta$. Uncertainties in the modelling of the jet energy resolution (JER) also contribute and are estimated from collision data. Additional uncertainties arise from the modelling of jets with $p_T < 20$ GeV as well as from soft energy deposits in the calorimeter that are not associated with reconstructed physics objects. Other minor uncertainties are assigned to the reconstruction of $E_T^{miss}$ and to account for the impact of pile-up collisions on $E_T^{miss}$.

**Lepton modelling**   Uncertainties in the electron and muon reconstruction, identification, and trigger efficiencies are estimated using tag-and-probe methods on samples enriched with $Z \rightarrow \ell\ell$, $J/\psi \rightarrow \ell\ell$, or $W^\pm \rightarrow \ell\nu$ ($\ell = e, \mu$) events. Other components include the electron and muon energy scale.

**Luminosity**   The uncertainty on the integrated luminosity is 3.6%. It is derived, following the same methodology as that detailed in Ref. [61], from a preliminary calibration of the luminosity scale derived from beam-separation scans performed in April 2012.

**PDFs**   The systematic uncertainties related to the parton distribution functions are taken into account for all samples using simulated events. The events are reweighted according to each of the PDF uncertainty eigenvectors. The uncertainties are calculated using the formula given in Equation 43 of Ref. [62]. The envelope is calculated, following the PDF4LHC recommendation, of the estimated uncertainties for the CT10 PDF set, the MSTW2008nlo [63] PDF set, and the NNPDF2.0 [64] set as final PDF uncertainty.

**Generator and parton shower**   Uncertainties in the modelling of the event kinematics with Monte Carlo generators are taken into account for the top-quark background and the diboson background. The uncertainty due to the choice of POWHEG as generator for the diboson background is estimated by comparing the event rate and the shape of the NN discriminants to the ones obtained with MC@NLO. The generator uncertainty on the $t\bar{t}$ background is estimated by comparing MC@NLO and ALPGEN. In addition, uncertainties are assigned to the modelling of the parton showers and hadronisation by interchanging the modelling between PYTHIA and HERWIG.

**Pile-up**   The uncertainty on the modelling of pile-up events is determined by varying the average number of collisions per bunch crossing in simulated events.

**MC statistics**    The impact of using simulation samples of limited size is also taken into account. This is done by generating pseudo-experiments, where the probability density of the NN discriminants (templates) is varied within their statistical uncertainty.

**Background rates**    The rate of top-quark background is normalised using the event yield in a control region as one component in the maximum-likelihood fit. However, when generating the pseudo-experiments for the statistical analysis the theoretical cross-section uncertainty of 22% is taken into account. The $W$+jets background arises from a jet being misidentified as a lepton. The uncertainty on understanding the misidentification rate and the resulting $W$+jets event rate is 43% in the 0-jet channel and 41% in the 2-jet channel (see section 3). The diboson and $Z$+jets backgrounds are normalised according to the cross sections predicted by theoretical computations and the corresponding uncertainties are quoted in Table 3.

**Signal cross-section**    The relative uncertainty on the signal cross sections (gluon fusion, VBF and *WH/ZH*) is determined following Ref. [65, 66]. The relative cross-section uncertainty of these processes is assumed to be 25% for gluon fusion in the 0-jet channel and 30% in the 2-jet channel, while the uncertainty on the combined VBF/*WH/ZH* category is 10%. These uncertainties also account for uncertainties in the modelling of the underlying event. The cross-section uncertainties in the gluon-fusion process are treated uncorrelated between the 0-jet channel and the 2-jet channel, since they arise from different sources.

The rate and cross-section uncertainties of the background processes that are modelled based on simulated events are summarised in Table 3.

Table 3: Relative systematic rate uncertainties for background processes in the 0-jet channel and the 2-jet channel. The uncertainties are rounded to full per cent, but all uncertainties that are smaller than 1% are rounded up. As described in the text above, the exact value of the luminosity uncertainty is 3.6% for each process. DY stands for Drell-Yan processes and the single top-quark processes are denoted $Wt/tq/t\bar{b}$.

| Process | | $WW/WZ/ZZ/W\gamma/W\gamma^*$ | $t\bar{t}/Wt/tq/t\bar{b}$ | DY/Z+jets |
|---|---|---|---|---|
| Jet modelling | 0-jet bin | 3% | 14% | 10% |
| | 2-jet bin | 11% | 37% | 12% |
| Lepton modelling | 0-jet bin | 2% | 2% | 6% |
| | 2-jet bin | 2% | 2% | 2% |
| Lumi | 0-jet bin | 4% | 4% | 4% |
| | 2-jet bin | 4% | 4% | 4% |
| PDF | 0-jet bin | 6% | 6% | 6% |
| | 2-jet bin | 5% | 7% | 5% |
| Generator | 0-jet bin | 1% | 3% | – |
| | 2-jet bin | 2% | 22% | – |
| Pile-up modelling | 0-jet bin | 2% | 1% | 2% |
| | 2-jet bin | 1% | 1% | 1% |
| Parton Shower | 0-jet bin | – | 7% | – |
| | 2-jet bin | – | 13% | – |
| Total | 0-jet bin | 8% | 18% | 14% |
| | 2-jet bin | 13% | 46% | 14% |
| Cross section | | 25% | 22% | 34% |

# 6 Hypothesis tests

To estimate the signal content of the selected samples, a maximum-likelihood fit is performed to the NN output distributions and to the event yield in the $t\bar{t}$ control region. Including all bins of the NN output distributions in the fit has the advantage of making maximal use of all signal events remaining after the event selection, and, in addition, allows for constraining the background rates from the data. The likelihood fit is performed simultaneously in both signal channels, that is the 0-jet channel and the 2-jet channel, and in the $t\bar{t}$ control region where only the event yield is considered, since it is very pure and discrimination between different processes is not needed. The sensitivity to the background rates is given by the background dominated region of the NN output distribution, that is the region close to zero, and the event yield in the $t\bar{t}$ control region.

The likelihood function is given by the product of Poisson probability terms for the individual histogram bins. The background rates, except for the $t\bar{t}$ background, are constrained by Gaussian priors that are added multiplicatively to the likelihood function. Within the likelihood function the predicted signal and background rates are multiplied by scale factors $\beta^s$ for the signal and $\beta^b_j$ for the backgrounds, respectively; with the index $j$ running over all background processes.

## 6.1 The q-value test statistic

The compatibility of the observed data with the different signal hypotheses, which depend on the parameters of the 2HDM, and the background-only hypothesis is evaluated by performing frequentist hypotheses tests based on pseudo-experiments. Two hypotheses are compared. The null hypothesis $H_0$ assumes, that there is no Higgs boson at all. The signal hypothesis $H_1$ assumes a Higgs boson signal as predicted by a specific 2HDM, depending on the values of $\cos\alpha$, $\tan\beta$, and $m_H$. The Higgs-like boson observed at 125 GeV is part of the signal hypothesis, assuming that it is the $h$ of a 2HDM. The signal strength of the $h$ boson used in the statistical test is the one predicted by the 2HDM under consideration. In addition, the signal hypothesis includes the contribution of the $H$ boson. For both scenarios ensemble tests, that is large sets of pseudo-experiments, are performed. To distinguish between the two hypotheses the so-called $q$ value is used as a test statistic. It is defined as minus two times the difference of the logarithm of the maximum of the likelihood function evaluated when fixing the signal cross sections to their predicted values in 2HDM ($\beta^s_j = 1$) and found by setting the signal cross sections to zero ($\beta^s_j = 0$). The background scale factors $\beta^b_j$ are left free to float in both cases within their uncertainties. The two fits yield the two maxima $\mathcal{L}(\beta^s = 1, \hat{\hat{\beta}}^{b,1}_j)$ and $\mathcal{L}(\beta^s = 0, \hat{\hat{\beta}}^{b,0}_j)$, respectively, and the $q$ value is then defined as

$$q \equiv -2\ln\left(\mathcal{L}\left(\beta^s = 1, \hat{\hat{\beta}}^{b,1}_j\right) \Big/ \mathcal{L}\left(\beta^s = 0, \hat{\hat{\beta}}^{b,0}_j\right)\right). \tag{3}$$

The $q$ value is computed for each pseudo experiment done under the two hypotheses. Each time the pseudo data are fitted twice to obtain the two values of the likelihood function.

By running a large set of pseudo experiments one obtains the $q$-value distribution of the null hypothesis, denoted by $g_0(q)$, and the $q$-value distribution of the signal hypothesis $g_1(q)$. By normalising these distributions to have an area of unity, one obtains the probability densities $\hat{g}_0(q)$ and $\hat{g}_1(q)$.

To test the compatibility of the observed data with the two hypotheses $H_0$ and $H_1$, one computes the observed $q$-value $q^{obs}$ by fitting the discriminant distributions in data and compares $q^{obs}$ with the two probability densities $\hat{g}_0(q)$ and $\hat{g}_1(q)$.

## 6.2 Exclusion Limits

The $CL_s$ method [67, 68] is used to derive confidence levels (CL) for a certain value of $q^{obs}$. Based on the $q$-value probability densities $\hat{g}_0(q)$ and $\hat{g}_1(q)$ one first computes the background $p$-value, also referred to

as $p_b$, and the signal plus background $p_{s+b}$-value as follows:

$$p\left(q^{\text{obs}}\right) = \int_{-\infty}^{q^{\text{obs}}} \hat{g}_0\left(q'\right) dq' \tag{4}$$

$$p_{s+b}\left(q^{\text{obs}}\right) = \int_{q^{\text{obs}}}^{-\infty} \hat{g}_1\left(q'\right) dq' . \tag{5}$$

The definition of $\text{CL}_s$ is given by:

$$\text{CL}_s = \frac{p_{s+b}}{1 - p_b}. \tag{6}$$

Due to the denominator, the $\text{CL}_s$ method includes the sensitivity to distinguish between the considered hypotheses and thus avoids spurious exclusions. A particular signal hypothesis $H_1$, determined by a triplet of the 2HDM parameters $\cos\alpha$, $\tan\beta$, and $m_H$, is excluded at the 95% CL if one finds $\text{CL}_s < 0.05$.

# 7  Results

The hypotheses tests are performed for a large part of the 2HDM parameter space, considering type-I as well as type-II models. The mixing angle $\alpha$ is scanned in $\cos\alpha$ in steps of 0.1. The following values of $\tan\beta$ are considered: 1, 3, 6, 20, for type-I and type-II models and $\tan\beta = 50$ for type-I models only. For type-II models the highest $\tan\beta$ is not investigated since for some part of the parameter space the width of the Higgs boson becomes so large that the width used in the Monte Carlo simulation would no longer be valid. The mass range of $135 < m_H < 300$ GeV is considered for the mass of the CP-even Higgs boson $H$, avoiding the mass region close to the light Higgs boson at $m_h = 125$ GeV. The mass range is scanned in steps of 5 GeV from $m_H = 135$ GeV to 200 GeV and in steps of 20 GeV in the range from 200 GeV to 300 GeV. For each combination of these parameters the $\text{CL}_s$ values are determined and exclusion contours are drawn in the $\cos\alpha$–$m_H$ plane at the 95% CL. The results are given in Fig. 7 for type-I 2HDMs and in Fig. 8 for type-II 2HDMs. For further illustration exclusion contours at the 99% CL are also displayed.

In the mass region from 135 to 200 GeV a large part of the $\cos\alpha$–$m_H$ plane can be excluded. In type-I models with $\cos\alpha \approx 0$ and $\tan\beta = 1$ masses up to 250 GeV are excluded. For type-II models the excluded region shrinks strongly with increasing $\tan\beta$, since the branching fraction to the $WW$ final state decreases. The reason for this is that the couplings to third generation down-type fermions, namely the bottom quark and the tau lepton, scale with $\tan\beta$ in type-II models. As the branching fraction to $b\bar{b}$ and $\tau^+\tau^-$ final states increases, the branching fraction of the $WW$ channel decreases.

To get an understanding of the *a-priori* sensitivity of the analysis, the expected exclusion contours are also computed. In this calculation, the median $q_0$ of the $\hat{g}_0(q)$ distribution instead of $q^{\text{obs}}$ is used. In general, one finds a very good agreement between the expected and the observed exclusion. In most cases, the observed exclusion is slightly smaller than the expected one, since one finds an excess of events over the expectation. This is particularly true when approaching the mass region close to the observed Higgs-like boson at 125 GeV, which was not included in the null hypothesis. Not including it makes the background estimate lower and the expected limits are therefore less constraining.

# 8  Conclusion

The analysis presented in this note hypothesises that the Higgs-like boson $h$ observed by the LHC experiments at $m_h \approx 125$ GeV is part of a 2HDM. Following this hypothesis, a search for a second, heavier, CP-even scalar boson $H$, has been performed, including the new boson $h$ as part of the 2HDM
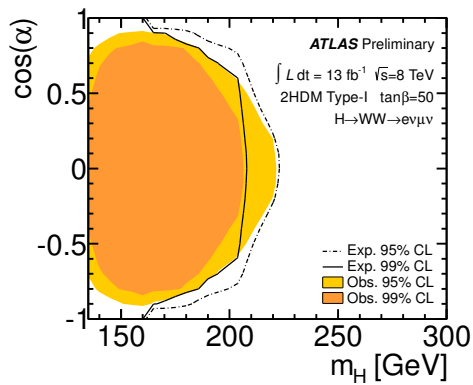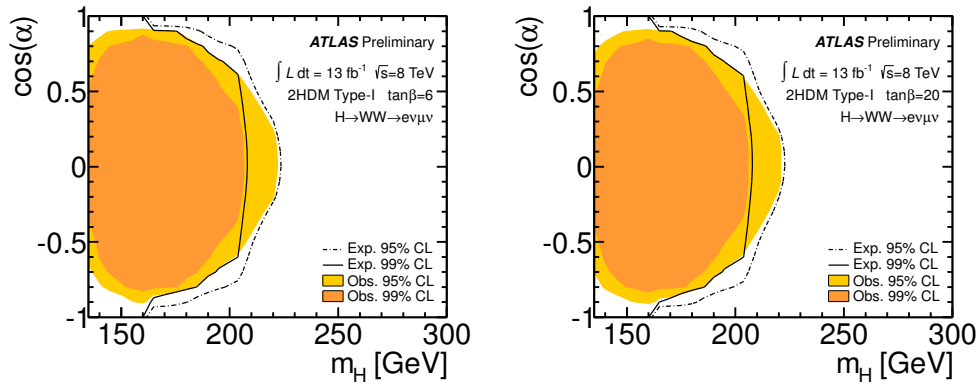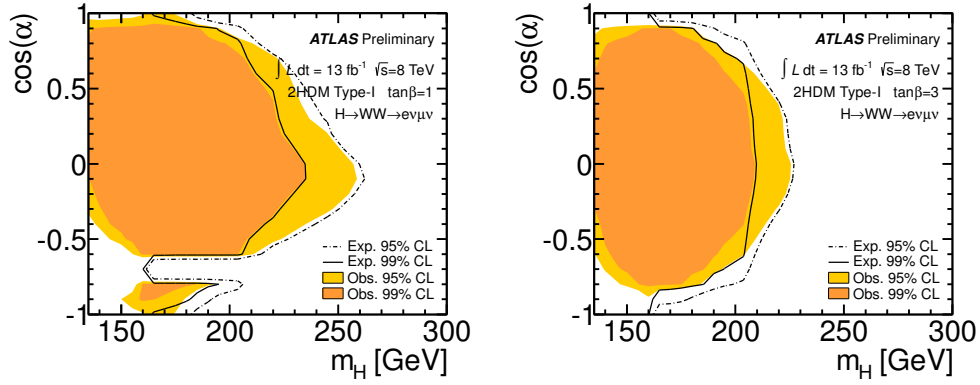
(a)



(b)



(c)



(d)



(e)

Figure 7: Exclusion contours in the $\cos\alpha$–$m_H$ plane for type-I 2HDMs.
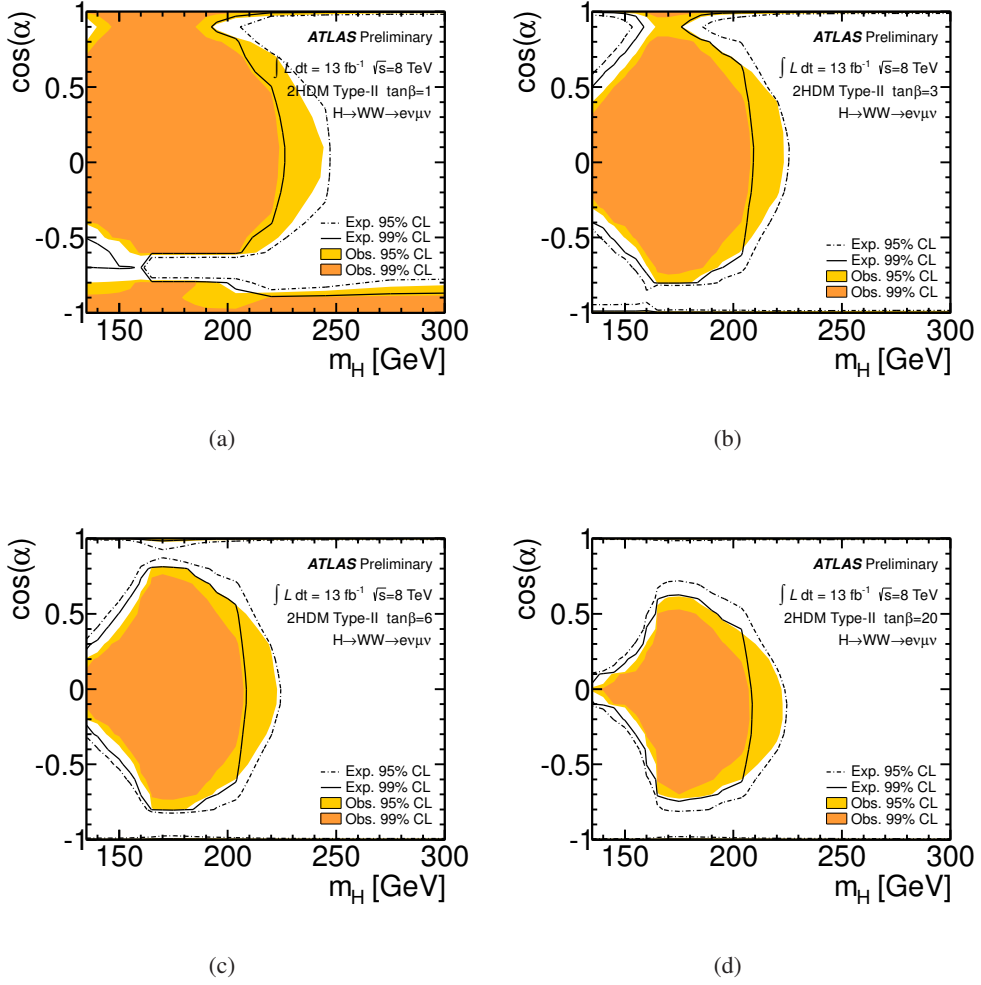
Figure 8: Exclusion contours in the $\cos\alpha$–$m_H$ plane for type-II 2HDMs.

signal model and comparing it to a background only model. Both bosons are reconstructed in the $h/H \to WW^{(*)} \to e\nu\mu\nu$ decay channel and contribute to the signal rate. The collision data at a centre-of-mass energy of 8 TeV were recorded with the ATLAS detector and correspond to an integrated luminosity of $13.0\,\mathrm{fb}^{-1}$. No evidence for an additional Higgs boson $H$ is found in the investigated mass range of $135 < m_H < 300$ GeV and exclusion contours at the 95% and 99% CL are determined in the $\cos\alpha$-$m_H$ plane for different values of $\tan\beta$ ranging from 1 to 50. In the mass region from 135 to 200 GeV a large part of the $\cos\alpha$-$m_H$ plane can be excluded for type-I 2HDMs.

# References

[1] ATLAS Collaboration, *Observation of a new particle in the search for the Standard Model Higgs boson with the ATLAS detector at the LHC*, Phys.Lett. **B716** (2012) 1–29, `arXiv:1207.7214 [hep-ex]`.

[2] CMS Collaboration, *Observation of a new boson at a mass of 125 GeV with the CMS experiment at the LHC*, Phys.Lett. **B716** (2012) 30–61, `arXiv:1207.7235 [hep-ex]`.

[3] ALEPH Collaboration, CDF Collaboration, D0 Collaboration, DELPHI Collaboration, L3 Collaboration, OPAL Collaboration, SLD Collaboration, LEP Electroweak Working Group, Tevatron Electroweak Working Group, SLD Electroweak and Heavy Flavour Groups Collaboration, *Precision electroweak measurements and constraints on the Standard Model*, `arXiv:1012.2367`.

[4] F. Englert and R. Brout, *Broken symmetry and the mass of gauge vector mesons*, Phys. Rev. Lett. **13** (1964) 321–322.

[5] P. W. Higgs, *Broken symmetries and the masses of gauge bosons*, Phys. Rev. Lett. **13** (1964) 508–509.

[6] G. S. Guralnik, C. R. Hagen, and T. W. B. Kibble, *Global conservation laws and massless particles*, Phys. Rev. Lett. **13** (1964) 585–587.

[7] T. Lee, *A theory of spontaneous T violation*, Phys.Rev. **D8** (1973) 1226–1239.

[8] M. Trodden, *Electroweak baryogenesis: A brief review*, `arXiv:hep-ph/9805252 [hep-ph]`.

[9] J. E. Kim, *Light pseudoscalars, particle physics and cosmology*, Phys. Rept. **150** (1987) 1–177.

[10] H. E. Haber and G. L. Kane, *The search for supersymmetry: probing physics beyond the Standard Model*, Phys. Rept. **117** (1985) 75–263.

[11] G. Branco, P. Ferreira, L. Lavoura, M. Rebelo, M. Sher, et al., *Theory and phenomenology of two-Higgs-doublet models*, Phys.Rept. **516** (2012) 1–102, `arXiv:1106.0034 [hep-ph]`.

[12] A. Djouadi, *The Anatomy of electro-weak symmetry breaking. II. The Higgs bosons in the minimal supersymmetric model*, Phys.Rept. **459** (2008) 1–241, `arXiv:hep-ph/0503173 [hep-ph]`.

[13] C.-Y. Chen and S. Dawson, *Exploring two-Higgs-doublet models through Higgs production*, `arXiv:1301.0309 [hep-ph]`.

[14] J. Chang, K. Cheung, P.-Y. Tseng, and T.-C. Yuan, *Implications on the heavy CP-even Higgs boson from current Higgs data*, `arXiv:1211.3849 [hep-ph]`.

[15] A. Drozd, B. Grzadkowski, J. F. Gunion, and Y. Jiang, *Two-Higgs-doublet models and enhanced rates for a 125 GeV Higgs*, `arXiv:1211.3580 [hep-ph]`.

[16] W. Altmannshofer, S. Gori, and G. D. Kribs, *A minimal-flavor-violating 2HDM at the LHC*, Phys. Rev. **D86** (2012) 115009, `arXiv:1210.2465 [hep-ph]`.

[17] D. S. Alves, P. J. Fox, and N. J. Weiner, *Higgs signals in a type-I 2HDM or with a sister Higgs*, `arXiv:1207.5499 [hep-ph]`.

[18] CDF Collaboration, T. Aaltonen et al., *Search for a two-Higgs-boson doublet using a simplified model in $p\bar{p}$ collisions at $\sqrt{s} = 1.96$ TeV*, arXiv:1212.3837 [hep-ex].

[19] CDF Collaboration, T. Aaltonen et al., *Search for Higgs bosons predicted in two-Higgs-doublet models via decays to tau lepton pairs in 1.96-TeV p anti-p collisions*, Phys.Rev.Lett. **103** (2009) 201801, arXiv:0906.1014 [hep-ex].

[20] P. Ferreira, R. Santos, M. Sher, and J. P. Silva, *Implications of the LHC two-photon signal for two-Higgs-doublet models*, Phys.Rev. **D85** (2012) 077703, arXiv:1112.3277 [hep-ph].

[21] The ATLAS Collaboration, *The ATLAS experiment at the CERN Large Hadron Collider*, J. Inst. **3** (2008) S08003.

[22] P. N. S. Alioli, C. Oleari, and E. Re, *NLO Higgs boson production via gluon fusion matched with shower in POWHEG*, JHEP **0904** (2009) 002, arXiv:0812.0578 [hep-ph].

[23] P. Nason and C. Oleari, *NLO Higgs boson production via vector-boson fusion matched with shower in POWHEG*, JHEP **1002** (2010) 037, arXiv:0911.5299 [hep-ph].

[24] S. M. T. Sjostrand and P. Z. Skands, *PYTHIA 6.4 physics and manual*, JHEP **0605** (2006) 026.

[25] H.-L. Lai et al., *New parton distributions for collider physics*, Phys. Rev. **D82** (2010) 074024, arXiv:1007.2241 [hep-ph].

[26] R. V. Harlander and W. B. Kilgore, *Next-to-next-to-leading order Higgs production at hadron colliders*, Phys.Rev.Lett. **88** (2002) 201801, arXiv:hep-ph/0201206 [hep-ph].

[27] C. Anastasiou and K. Melnikov, *Higgs boson production at hadron colliders in NNLO QCD*, Nucl.Phys. **B646** (2002) 220–256, arXiv:hep-ph/0207004 [hep-ph].

[28] V. Ravindran, J. Smith, and W. L. van Neerven, *NNLO corrections to the total cross-section for Higgs boson production in hadron hadron collisions*, Nucl.Phys. **B665** (2003) 325–366, arXiv:hep-ph/0302135 [hep-ph].

[29] U. Aglietti, R. Bonciani, G. Degrassi, and A. Vicini, *Two loop light fermion contribution to Higgs production and decays*, Phys. Lett. **B595** (2004) 432–441, arXiv:hep-ph/0404071 [hep-ph].

[30] S. Actis, G. Passarino, C. Sturm, and S. Uccirati, *NLO electroweak corrections to Higgs boson production at hadron colliders*, Phys. Lett. **B670** (2008) 12–17, arXiv:0809.1301 [hep-ph].

[31] S. Catani, D. de Florian, M. Grazzini, and P. Nason, *Soft gluon resummation for Higgs boson production at hadron colliders*, JHEP **0307** (2003) 028, arXiv:hep-ph/0306211 [hep-ph].

[32] R. V. Harlander, S. Liebler, and H. Mantler, *SusHi: A program for the calculation of Higgs production in gluon fusion and bottom-quark annihilation in the Standard Model and the MSSM*, arXiv:1212.3249 [hep-ph].

[33] G. Degrassi, S. Di Vita, and P. Slavich, *On the NLO QCD corrections to the production of the heaviest neutral Higgs scalar in the MSSM*, Eur. Phys. J. **C72** (2012) 2032, arXiv:1204.1016 [hep-ph].

[34] M. Ciccolini, A. Denner, and S. Dittmaier, *Strong and electroweak corrections to the production of Higgs + 2 jets via weak interactions at the LHC*, Phys. Rev. Lett. **99** (2007) 161803, arXiv:0707.0381 [hep-ph].

[35] M. Ciccolini, A. Denner, and S. Dittmaier, *Electroweak and QCD corrections to Higgs production via vector-boson fusion at the LHC*, Phys.Rev. **D77** (2008) 013002, `arXiv:0710.4749 [hep-ph]`.

[36] K. Arnold, M. Bahr, G. Bozzi, F. Campanario, C. Englert, et al., *VBFNLO: A parton level Monte Carlo for processes with electroweak bosons*, Comput.Phys.Commun. **180** (2009) 1661–1670, `arXiv:0811.4559 [hep-ph]`.

[37] P. Bolzoni, F. Maltoni, S.-O. Moch, and M. Zaro, *Higgs production via vector-boson fusion at NNLO in QCD*, Phys.Rev.Lett. **105** (2010) 011801, `arXiv:1003.4451 [hep-ph]`.

[38] O. Brein, A. Djouadi, and R. Harlander, *NNLO QCD corrections to the Higgs-strahlung processes at hadron colliders*, Phys.Lett. **B579** (2004) 149–156, `arXiv:hep-ph/0307206 [hep-ph]`.

[39] M. Ciccolini, S. Dittmaier, and M. Kramer, *Electroweak radiative corrections to associated WH and ZH production at hadron colliders*, Phys.Rev. **D68** (2003) 073003, `arXiv:hep-ph/0306234 [hep-ph]`.

[40] M. L. Mangano et al., *ALPGEN, a generator for hard multi-parton processes in hadronic collisions*, JHEP **0307** (2003) 001.

[41] G. Corcella et al., *HERWIG 6: an event generator for hadron emission reactions with interfering gluons (including super-symmetric processes)*, JHEP **0101** (2001) 010.

[42] J. Butterworth, J. R. Forshaw, and M. Seymour, *Multiparton interactions in photoproduction at HERA*, Z.Phys. **C72** (1996) 637–646, `arXiv:hep-ph/9601371 [hep-ph]`.

[43] J. Alwall et al., *Comparative study of various algorithms for the merging of parton showers and matrix elem ents in hadronic collisions*, Eur. Phys. J. **C53** (2008) 473–500. `doi:10.1140/epjc/s10052-007-0490-5`.

[44] T. Binoth, M. Ciccolini, N. Kauer and M. Krämer, *Gluon-induced W-boson pair production at the LHC*, JHEP **12** (2006) 046, `hep-ph/0611170v1`.

[45] J. Alwall et al., *MadGraph/MadEvent v4: The new web generation*, JHEP **0709** (2007) 028, `arXiv:0706.2334 [hep-ph]`.

[46] B. P. Kersevan and E. Richter-Was, *The Monte Carlo event generator AcerMC version 2.0 with interfaces to PYTHIA 6.2 and HERWIG 6.5*, arXiv:hep-ph/0405247 (2004) .

[47] S. Frixione and B. Webber, *Matching NLO QCD and parton showers in heavy-flavor production*, JHEP **0308** (2003) 007.

[48] ATLAS Collaboration, *Update of the $H \rightarrow WW^{(*)} \rightarrow e\nu\mu\nu$ Analysis with 13 $fb^{-1}$ of $\sqrt{s} = 8$ TeV Data Collected with the ATLAS Detector*, ATLAS-CONF-2012-158, available at https://cds.cern.ch/record/1493601.

[49] ATLAS Collaboration, *The ATLAS Simulation Infrastructure*, Eur. Phys. J. **C70** (2010) 823–874, `arXiv:1005.4568 [hep-ex]`.

[50] S. Agostinelli et al., *GEANT 4, A Simulation Toolkit*, Nucl. Instrum. Meth. **A506** (2003) 250–303.

[51] ATLAS Collaboration, *Improved electron reconstruction in ATLAS using the Gaussian sum filter-based model for bremsstrahlung*, ATLAS-CONF-2012-047, available at https://cds.cern.ch/record/1449796.

[52] M. Cacciari, G. P. Salam, and G. Soyez, *The anti-$k_t$ jet clustering algorithm*, JHEP **0804** (2008) 063, `arXiv:0802.1189 [hep-ph]`.

[53] ATLAS Collaboration, *Update on the jet energy scale systematic uncertainty for jets produced in proton-proton collisions at $\sqrt{s}$ = 7 TeV measured with the ATLAS detector*, ATLAS-CONF-2011-007, available at https://cds.cern.ch/record/1330713.

[54] ATLAS Collaboration, *Measurement of the b-tag efficiency in a sample of jets containing muons with 5 $fb^{-1}$ of data from the ATLAS detector*, ATLAS-CONF-2012-043, available at https://cds.cern.ch/record/1435197.

[55] ATLAS Collaboration, *Performance of the missing transverse energy reconstruction and calibration in pro ton-proton collisions at a center-of-mass energy of $\sqrt{s}$ = 7 TeV with the ATLAS detector*, ATLAS-CONF-2010-057, available at https://cds.cern.ch/record/1281330.

[56] M. Feindt and U. Kerzel, *The NeuroBayes neural network package*, Nucl. Instrum. Meth. A **559** (2006) 190–194.

[57] ATLAS Collaboration, *Measurement of the t-channel single top-quark production cross section in pp collisions at $\sqrt{s}$ = 7 TeV with the ATLAS detector*, Phys.Lett. **B717** (2012) 330–350, `arXiv:1205.3130 [hep-ex]`.

[58] D. Casadei and G. Choudalakis, *Plotting the differences between data and expectation*, Eur. Phys. J. Plus **127** (2012) 25.

[59] ATLAS Collaboration, *Jet energy measurement with the ATLAS detector in proton-proton collisions at sqrt(s) = 7 TeV*, `arXiv:1112.6426 [hep-ex]`.

[60] ATLAS Collaboration, *Commissioning of the ATLAS high-performance b-tagging algorithms in the 7 TeV collision data*, ATLAS-CONF-2011-102, available at https://cdsweb.cern.ch/record/1369219.

[61] ATLAS Collaboration, G. Aad et al., *Improved luminosity determination in pp collisions at sqrt(s) = 7 TeV using the ATLAS detector at the LHC*, `arXiv:1302.4393 [hep-ex]`.

[62] J. M. Campbell, J. Huston, and W. Stirling, *Hard interactions of quarks and gluons: A primer for LHC physics*, Rept. Prog. Phys. **70** (2007) 89–193, `arXiv:hep-ph/0611148`.

[63] A. Martin, W. Stirling, R. Thorne, and G. Watt, *Parton distributions for the LHC*, Eur. Phys. J. **C63** (2009) 189–285, `arXiv:0901.0002`.

[64] R. D. Ball, V. Bertone, F. Cerutti, L. Del Debbio, S. Forte, et al., *Impact of heavy-quark masses on parton distributions and LHC phenomenology*, Nucl. Phys. **B849** (2011) 296–363, `arXiv:1101.1300`.

[65] LHC Higgs Cross Section Working Group, S. Dittmaier, C. Mariotti, G. Passarino, and R. Tanaka (Eds.), *Handbook of LHC Higgs cross sections: 1. Inclusive observables*, CERN-2011-002 (CERN, Geneva, 2011), `arXiv:1101.0593 [hep-ph]`.

[66] LHC Higgs Cross Section Working Group, S. Dittmaier, C. Mariotti, G. Passarino, and R. Tanaka (Eds.), *Handbook of LHC Higgs cross sections: 2. Differential distributions*, CERN-2012-002 (CERN, Geneva, 2012), `arXiv:1201.3084 [hep-ph]`.

[67] T. Junk, *Confidence level computation for combining searches with small statistics*, Nucl. Instrum. Methods **A434** (1999) 435–443.

[68] A. L. Read, *Presentation of search results: the CL$_s$ technique*, J. Phys. G: Nucl. Part. Phys. **28** (2002) 2693–2704.
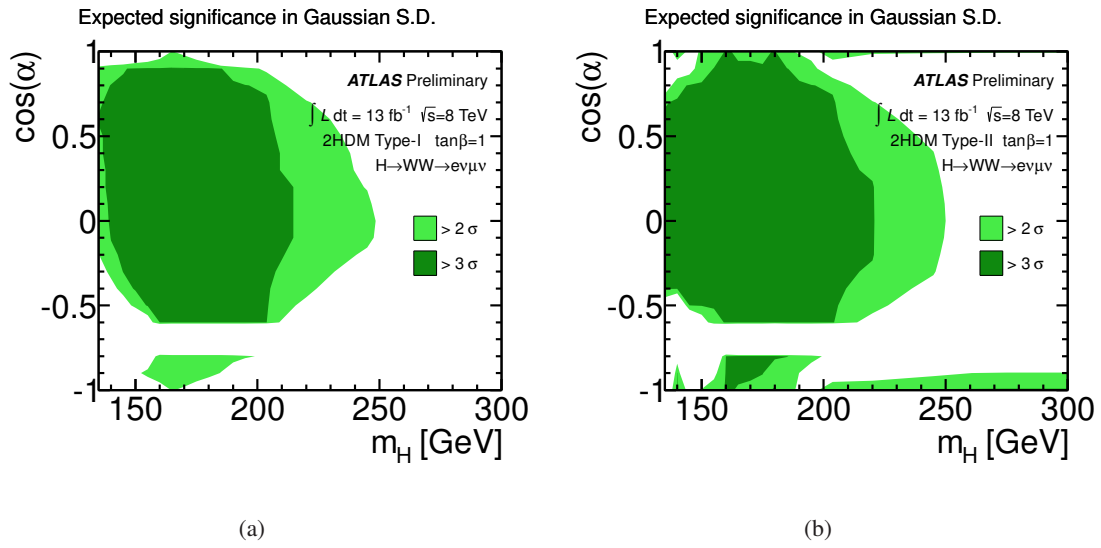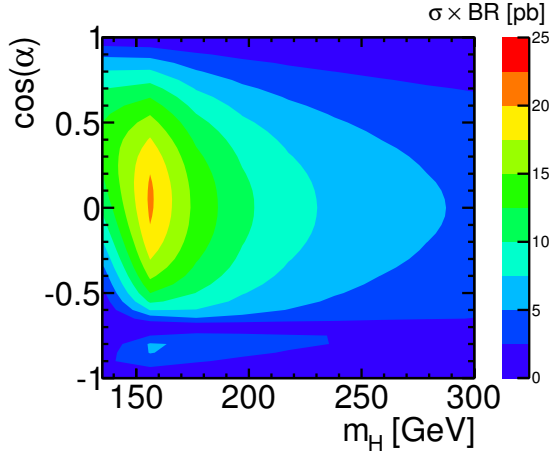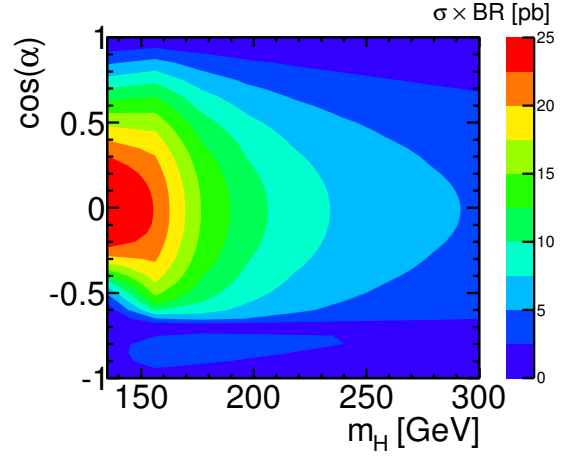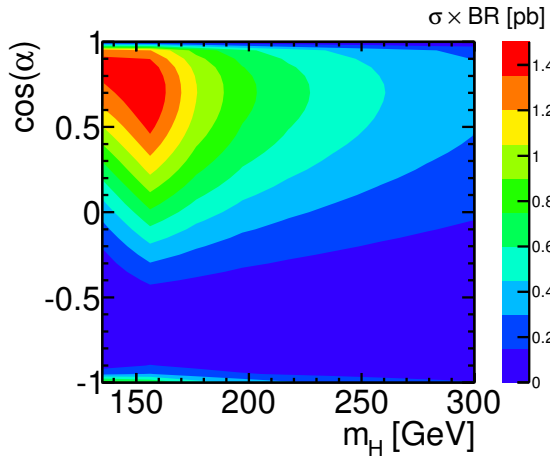
# Appendix



Figure 9: Contour plots of expected significance in Gaussian standard deviations for a type-I model (a) and a type-II model (b). The SM Higgs boson is included as part of the null hypothesis.
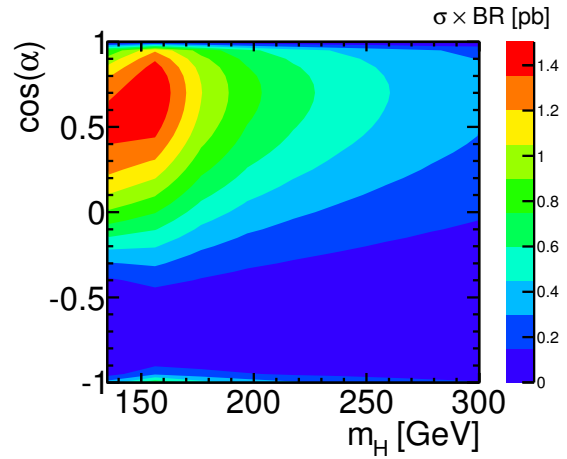
(a) Type-I, *gg* fusion, $\tan\beta = 1$

(b) Type-II, *gg* fusion, $\tan\beta = 1$

(c) Type-I, VBF, $\tan\beta = 1$

(d) Type-II, VBF, $\tan\beta = 1$

Figure 10: Cross section times branching ratio for the 2HDMs type-I and type-II in pb in the $\cos\alpha$-$m_H$ plane for $\tan\beta = 1$. Fig. (a) and (b) show the gluon fusion cross sections, fig. (c) and (d) show the VBF cross sections. The cross sections were calculated with *SusHi* [32].
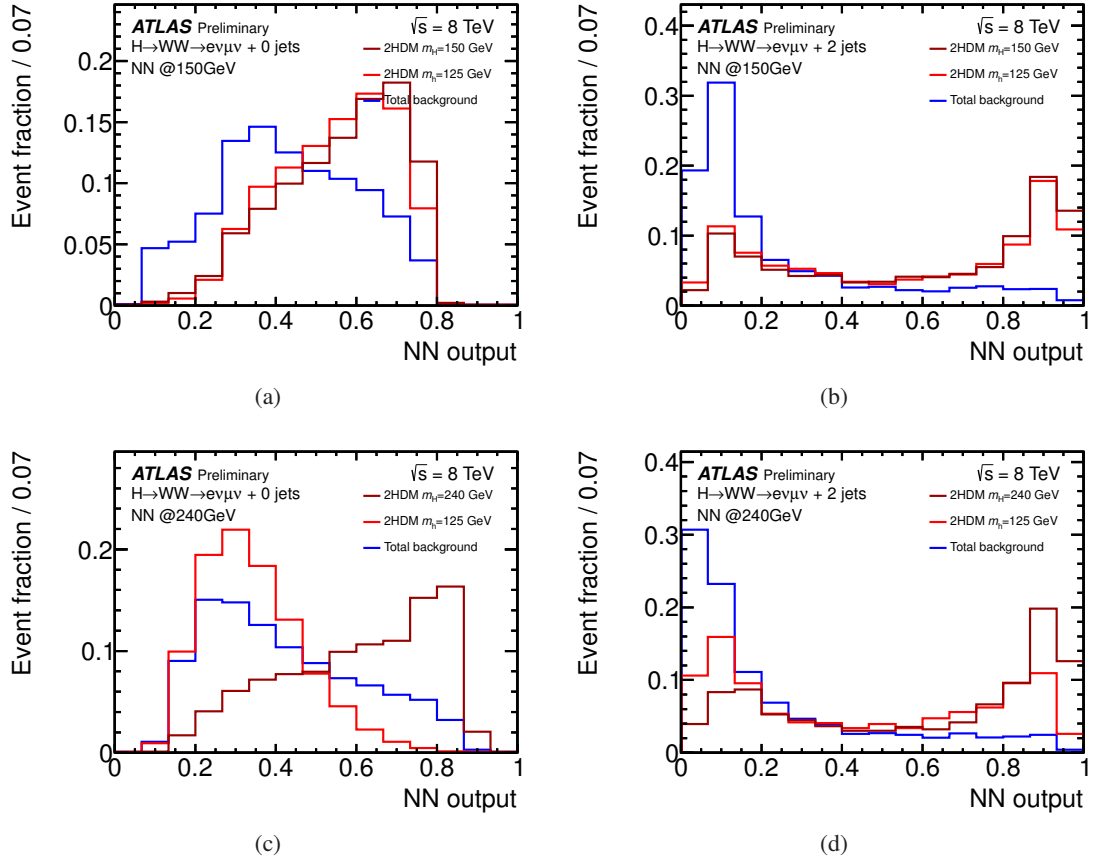
Figure 11: Normalised discriminant distributions (templates) obtained for the NNs optimised at $m_H$ = 150 GeV and $m_H$ = 240 GeV for the 2HDM signal and background, (a) and (c) in the 0-jet channel, and (b) and (d) in the 2-jet channel. The distributions are normalised to unit area.
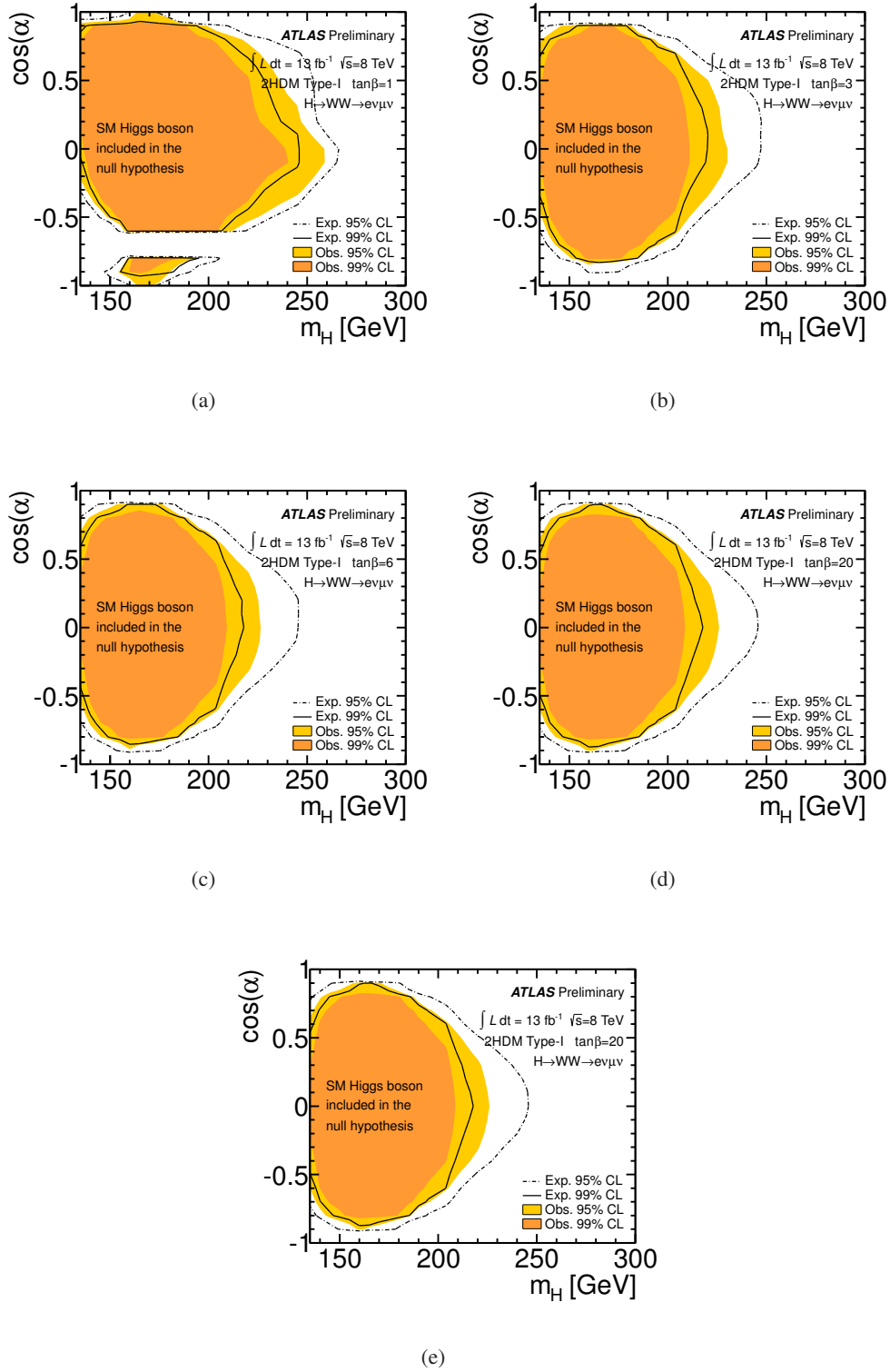
Figure 12: Exclusion contours in the $\cos\alpha$–$m_H$ plane for type-I 2HDMs. The SM Higgs boson is included in the null hypothesis.
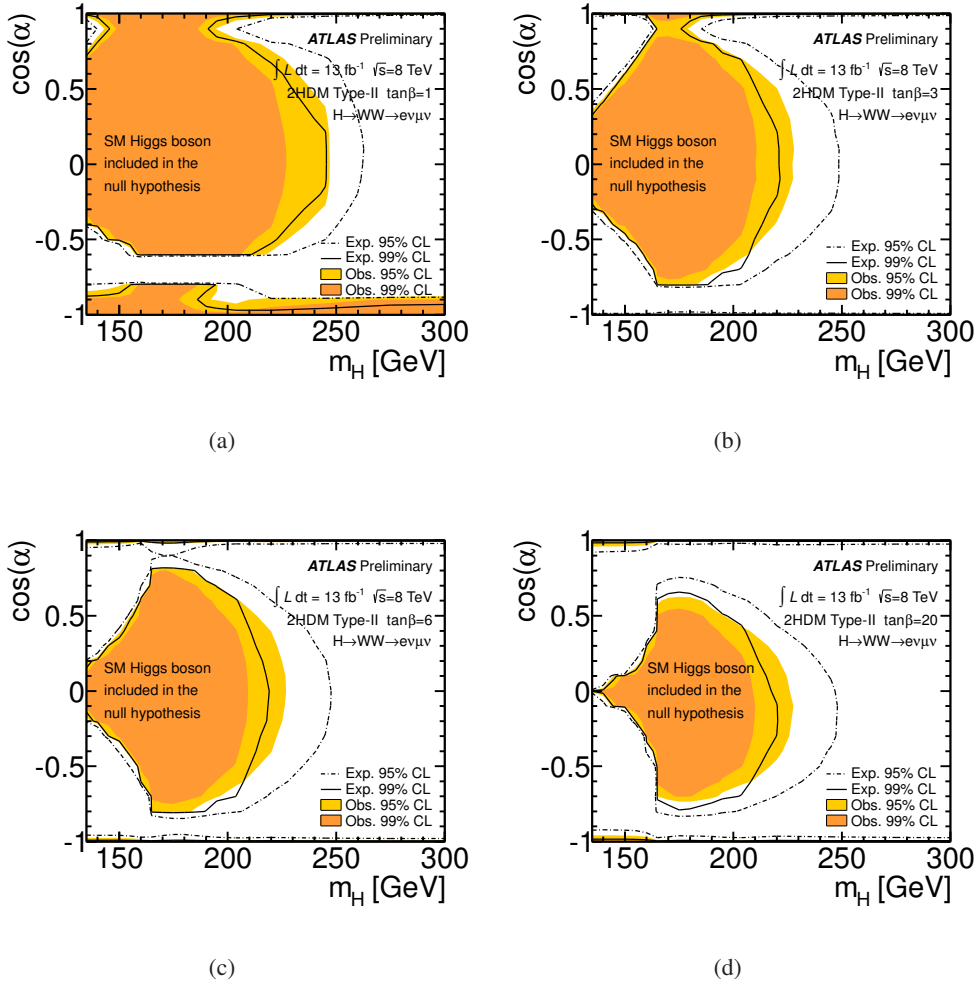
Figure 13: Exclusion contours in the $\cos\alpha$–$m_H$ plane for type-II 2HDMs. The SM Higgs boson is included in the null hypothesis.